LETTER

Chasing acyl carrier protein through a catalytic cycle of lipid A production

Ali Masoudi[1], Christian R. H. Raetz[1]‡, Pei Zhou[1] & Charles W. Pemble IV[2,3]

Acyl carrier protein represents one of the most highly conserved proteins across all domains of life and is nature's way of transporting hydrocarbon chains *in vivo*. Notably, type II acyl carrier proteins serve as a crucial interaction hub in primary cellular metabolism[1] by communicating transiently between partner enzymes of the numerous biosynthetic pathways[2,3]. However, the highly transient nature of such interactions and the inherent conformational mobility of acyl carrier protein[2] have stymied previous attempts to visualize structurally acyl carrier protein tied to an overall catalytic cycle. This is essential to understanding a fundamental aspect of cellular metabolism leading to compounds that are not only useful to the cell, but also of therapeutic value. For example, acyl carrier protein is central to the biosynthesis of the lipid A (endotoxin) component of lipopolysaccharides in Gram-negative microorganisms, which is required for their growth and survival[4,5], and is an activator of the mammalian host's immune system[6,7], thus emerging as an important therapeutic target[8–10]. During lipid A synthesis (Raetz pathway), acyl carrier protein shuttles acyl intermediates linked to its prosthetic 4′-phosphopantetheine group[2] among four acyltransferases, including LpxD[11]. Here we report the crystal structures of three forms of *Escherichia coli* acyl carrier protein engaging LpxD, which represent stalled substrate and liberated products along the reaction coordinate. The structures show the intricate interactions at the interface that optimally position acyl carrier protein for acyl delivery and that directly involve the pantetheinyl group. Conformational differences among the stalled acyl carrier proteins provide the molecular basis for the association–dissociation process. An unanticipated conformational shift of 4′-phosphopantetheine groups within the LpxD catalytic chamber shows an unprecedented role of acyl carrier protein in product release.

Although the paradigm for acyl carrier protein (ACP) association with protein partners is thought to be exceedingly transient, the LpxD acyltransferase in the Raetz pathway (Supplementary Fig. 1a) binds ACP with very high affinity ($K_d = 59$ nM)[12]. LpxD transfers *R*-3-hydroxymyristoyl (β-OH-C14) acyl chains that are delivered by ACP to the amino group of uridine diphosphate 3-O-(β-OH-C14)-α-D-glucosamine (UDP-acyl-GlcN)[12] (Supplementary Fig. 1b). Moreover, LpxD follows an ordered sequential kinetic mechanism in which acyl-ACP binds first and, importantly, holo-ACP (acyl chain has been liberated) dissociates last[12]. Given the canonical mode of ACP-mediated transfer often allows the rapid exchange between protein partners[13], such pronounced association between ACP and LpxD is most unusual and instead suggests a 'strong, transient'[14] interaction that would require a yet to be identified 'molecular trigger' for dissociation. Thus, we reasoned that the crystallographic study of the ACP–LpxD complex offers a unique opportunity to gain the detailed molecular basis for ACP-based acyl delivery and a deeper understanding of protein–protein communication more generally.

We present here three X-ray co-crystal structures of ACP bound to LpxD, each of which captured a different form of the carrier protein:

intact-acyl-ACP, hydrolysed-acyl-ACP and holo-ACP (Fig. 1a, b, Supplementary Fig. 2 and Supplementary Table 1). These structures were resolved to 2.1, 2.9 and 2.15 Å resolution, respectively (Supplementary Table 2). In each case, the triclinic unit cell contained two LpxD trimers with differing bound states of ACP (Supplementary Fig. 3). The overall B values for all ACPs modelled in each structure are two- to threefold higher than LpxD (Supplementary Fig. 4 and Supplementary Table 2) and, accordingly, the observed electron density was weaker in some regions (Supplementary Fig. 3). Nonetheless, the placement of side-chains at the protein–protein interface, prosthetic groups, and acyl chain(s) were apparent (Supplementary Fig. 2d–f and Supplementary Fig. 5). Our structures show the 4′-phosphopantetheine group (4′-PPT) (attached to Ser 36) and its β-OH-C14 acyl chains having vacated the canonical hydrophobic cavity extending through the core of ACP[2,15–17]—all of which require considerable movement (Supplementary Fig. 6). The overall architecture of the LpxD trimer is similar to previously reported X-ray structures[18,19] in that each monomer of LpxD can be subdivided into three domains (Fig. 1c and Supplementary Fig. 2): the amino (N)-terminal uridine-binding domain, which is tethered to the left-handed β-helix domain that harbours the conserved catalytic His 239 residue[12], and a carboxy (C)-terminal domain.

The structures show three molecules of the carrier protein are localized to the C-terminal end of LpxD (Fig. 1b). Notably, we have identified the ACP recognition domain (ARD) (Fig. 1c), which is formed by the C-terminal domain and the last beta-coil of the left-handed β-helix domain, providing the molecular basis for ACP association. This contrasts with a previous study that suggested the uridine-binding domain as the likely ACP docking site owing to its proximity to the catalytic cleft[18]. Although the analogous C-terminal region of the LpxA acyltransferase[20] is found to adopt a completely different orientation from that of LpxD, it may serve a similar function in binding ACP (Supplementary Fig. 7).
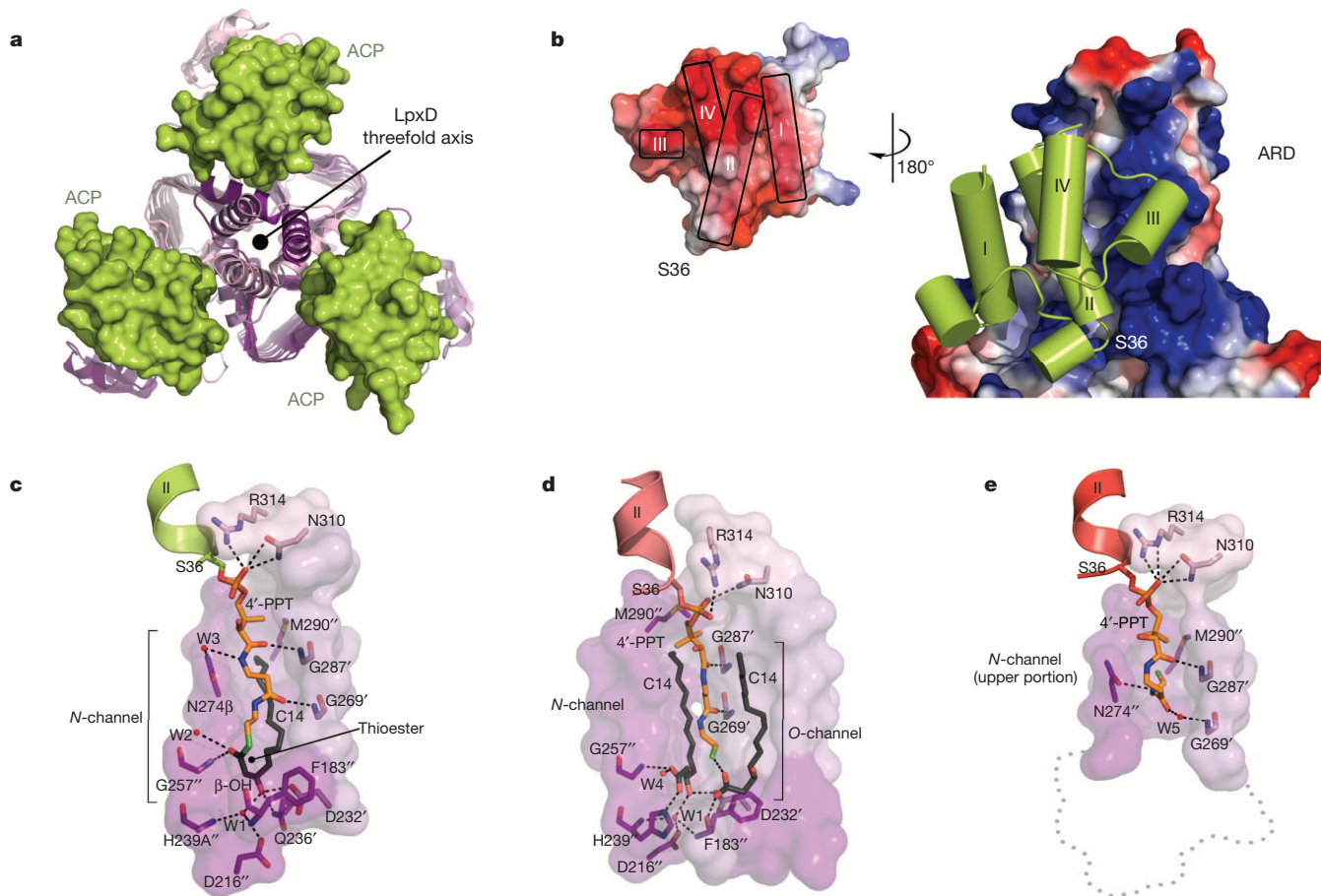
By virtue of the complete engagement of ACP, three competent active sites are created (Fig. 2a). Each ACP–LpxD interface buries a surface area of approximately 530 Å^2 and is predominated by complementary electrostatic interactions (Fig. 2b). In addition, van der Waals contacts and extensive interaction with the prosthetic group contribute to the large binding footprint that explains the 'strong, transient' nature of these two protein partners. A combination of residues located on the 'universal recognition helix' (helix II)[21], as well as portions of L1, L2 and helix-III of ACP, provide the acidic surface that binds a pronounced basic patch on LpxD. This surface feature of ACP can be subdivided into two highly acidic regions, I and II, which include residues Glu 30–Met 44 and Ala 45–Glu 60, respectively. The complementary binding surface on LpxD involves residues from all three monomers (denoted by prime symbols) and forms a shallow groove between coiled coils of the ARD into which helix-II packs (Supplementary Fig. 8).

Within region I, Asp 35, Ser 36, Leu 37, Asp 38, Val 40, Glu 41 and Met 44 are important for binding the N-terminal end of the recognition

[1]Department of Biochemistry, Duke University Medical Center, Durham, North Carolina 27710, USA. [2]Human Vaccine Institute, Duke University Medical Center, Durham, North Carolina 27710, USA. [3]Duke Macromolecular Crystallography Center, Duke University Medical Center, Durham, North Carolina 27710, USA.
‡Deceased.

helix to the base of the ARD domain (Supplementary Fig. 8), and the interactions were notably present in all three structures. Region II of ACP interacts with the upper portion of the ARD domain, the details of which differ substantially among the three stalled ACP complexes (discussed below). Most of the residues within regions I and II are conserved among other type II carrier proteins (Supplementary Fig. 2b) and have been implicated as key modulators of ACP association[22,23]. The most universal electrostatic interaction shown across the intact-, hydrolysed- and holo-ACP structures is between Arg 293 of LpxD and Asp 35, Asp 38 and Glu 41 of ACP that flank Ser 36. This coordination point is crucial for ACP association with LpxD as mutation of Arg 293 to alanine results in a 23-fold increase in Michaelis constant (K_m) for acyl-ACP compared with wild-type LpxD, with little effect on catalyst rate constant (k_{cat})[12]. These interactions orient ACP by positioning the pantetheinylated Ser 36 residue towards the catalytic chamber of LpxD.

In addition to the protein–protein interactions, the prosthetic group and acyl chain of intact-acyl-ACP extensively contact the surface of the partner enzyme (Supplementary Fig. 9). Inspection of the electron density indicates that the thioester scissile bond remained unbroken, which required a His239Ala LpxD variant (Supplementary Fig. 5a). The β-OH-C14 acyl chain and the 4′-PPT arm adopt a horseshoe-like conformation, which in effect buries the acyl chain between the prosthetic group and a pronounced hydrophobic channel (N-channel) formed between LpxD monomers (Fig. 2c). The 4′-phosphate moiety of 4′-PPT is directly coordinated by Asn 310 and Arg 314 of LpxD and may partly contribute to some level of specificity. The remainder of the 4′-PPT arm adopts a rather extended conformation, stretching over 14 Å, and interacts with residues primarily along the rim of the N-channel. This conformation places the thioester bond in proximity to the alanine-substituted His 239 catalytic base and orients the carbonyl-oxygen of β-OH-C14 towards the amide nitrogen atom of Gly 257″, corroborating its role in forming the oxyanion hole[12,24].

Two features of LpxD specificity towards β-hydroxyacyl chains are explained by the intact-acyl-ACP structure. First, the terminal two carbon atoms of β-OH-C14 pack against Met 290″ located at the far end of the N-channel (Fig. 2c and Supplementary Fig. 9). Given that LpxD is highly specific for 14-carbon acyl-chain-lengths[12], this supports the role of Met 290 as a 'hydrocarbon ruler'[19]. Second, LpxD is particularly selective for the β-hydroxyl group of the acyl chain; its removal completely abrogates acyltransferase activity[25]. Our structures show an intricate hydrogen bond network between the β-hydroxyl group and Asp 232′, Gln 236′ and a critical water-mediated bridge with Asp 216″ and the main-chain nitrogen atoms of Phe 183″ and His239Ala″.

By contrast to the intact-acyl-ACP complex, the thioester bond is broken in the hydrolysed-acyl-ACP structure (Fig. 2d, Supplementary Fig. 5b and Supplementary Fig. 9). Notably, we discovered a second molecule of β-OH-C14 fatty acid bound to the LpxD surface (Supplementary Fig. 10), which shows an extra hydrophobic channel (O-channel) that probably binds the acyl chain that is ester-linked to the UDP-acyl-GlcN lipid substrate (Supplementary Fig. 1b). A superposition with the previously reported *Chlamydia trachomatis* LpxD in complex with UDP-GlcNAc[18] illustrates the proximity of the carboxylate head group of the extra fatty acid to the anticipated binding locale of the 3-hydroxyl position of the GlcN ring (Supplementary Fig. 11).

What is striking about both the intact- and hydrolysed-acyl-ACP structures is the conformational similarity between the 4′-PPT prosthetic groups that are fully extended (Fig. 2c, d), whereas the holo-ACP structure shows an alternative conformation of its prosthetic group packing against the far end of the N-channel (Fig. 2e and Supplementary Fig. 9). Notably, in both intact- and hydrolysed-acyl-ACP the pantetheinyl arms completely enclose the reaction chambers (Fig. 3a). Although this architecture probably stabilizes substrate binding within the hydrophobic N-channel, it raises a key question. Given a sequential

Figure 2 | Intermolecular interactions between ACP and LpxD.
a, **b**, Overview of the protein–protein interactions (intact-acyl-ACP depicted). **a**, Top-down view of the ACP–LpxD complex showing three molecules of ACP bind per LpxD trimer. **b**, Electrostatic surface representation of the ARD and ACP (inset); the potential contours were scaled to +79.2 (blue) and −79.2 (red) $k_B T e^{-1}$ (where k_B is the Boltzmann constant, T is temperature and e^{-1} is the charge of an electron). **c**–**e**, Detailed interactions between the LpxD reaction chamber and the bound acyl/4′-PPT groups of ACP. Hydrogen bonds are shown as black dashes. Molecular surfaces are of only those residues that contribute to interactions. **c**, Intact-acyl-ACP complex. The β-OH-C14 acyl chain delivered by ACP binds the hydrophobic *N*-channel and its terminal carbon atoms pack near Met 290′′. **d**, Hydrolysed-acyl-ACP complex. An equivalent β-OH-C14 acyl chain is shown bound to a newly identified hydrophobic channel (*O*-channel). **e**, Holo-ACP complex. The 4′-PPT arm interacts at the far end of the *N*-channel, positioning the terminal thiol near Met 290′′. A 'ghost outline' of the catalytic cleft is indicated by a grey dotted line.

ordered reaction mechanism, how does the di-acylated-GlcN product leave LpxD before holo-ACP if the reaction chamber is completely blocked? A structural comparison between intact- and holo-ACP sheds light on this matter by exposing a substantial movement that the 4′-PPT arm has undergone (Fig. 3b). Notably, the terminal thiol of the 4′-PPT has vacated the catalytic cleft and moves approximately 15 Å to be situated near Met 290. A sizeable region of the reaction chamber closest to the catalytic cleft is now open to solvent, thereby giving the diacyl-GlcN product an opportunity to dissociate before the release of holo-ACP.

The remarkable difference in conformation shown by the 4′-PPT arm, together with the ordered sequential mechanism of acyl transfer, prompted us to propose that this 'swing' motion may in fact be involved in 'triggering' the release of lipid product. Because every terminal thiol of holo-ACP was positioned approximately 3.7 Å away from Met 290 of LpxD, we considered the possibility of mutating this residue to a cysteine in an effort to induce a mixed-disulphide linkage post-catalysis. Biochemically, the Met 290Cys mutation abrogates acyl transfer to UDP-acyl-GlcN compared with wild-type LpxD (Supplementary Fig. 12). This suggests that a covalent bond is formed between the cysteinyl and 4′-PPT thiols. Thus, we reasoned that the addition of reducing agent would rescue acyl transfer. Accordingly, titration of dithiothreitol (DTT) into the reaction mixture recovers activity of Met290Cys-LpxD to

levels indistinguishable from that of wild-type enzyme (Supplementary Fig. 12). These data suggest that the observed 4′-PPT motion has functional relevance in the course of product release. Moreover, as typically exemplified with 'strong, transient' interactions[14], this substantial movement of the pantetheine arm probably serves as the 'molecular trigger' that promotes the collapse of the ACP–partner complex.

Because our structures show different states of ACP stalled at the LpxD active site, an alignment of LpxD domains allows us to visualize the movements within ACP as it relates to the overall catalytic cycle (Fig. 3c), which to the best of our knowledge is unprecedented. Helix-I, helix-II and portions of L1 remain relatively unchanged (root mean squared deviation of approximately 1 Å) and are preserved for the purpose of remaining docked. The largest differences occur downstream of the recognition helix (Fig. 3c), including helices III, IV, L2 and L3 (root mean squared deviation of approximately 3 Å) and are an indication of what interactions must break for dissociation. A closer inspection shows that the intact-complex makes electrostatic interactions with the entire ARD interface that involves region II, whereas both the hydrolysed- and holo-ACP structures do not (Fig. 3d). These data indicate that the more extensive interactions are important for molecular recognition during association; however, after acyl transfer it is conformational changes in ACP that ultimately destabilize the protein–protein complex. In this context, one particular molecule of
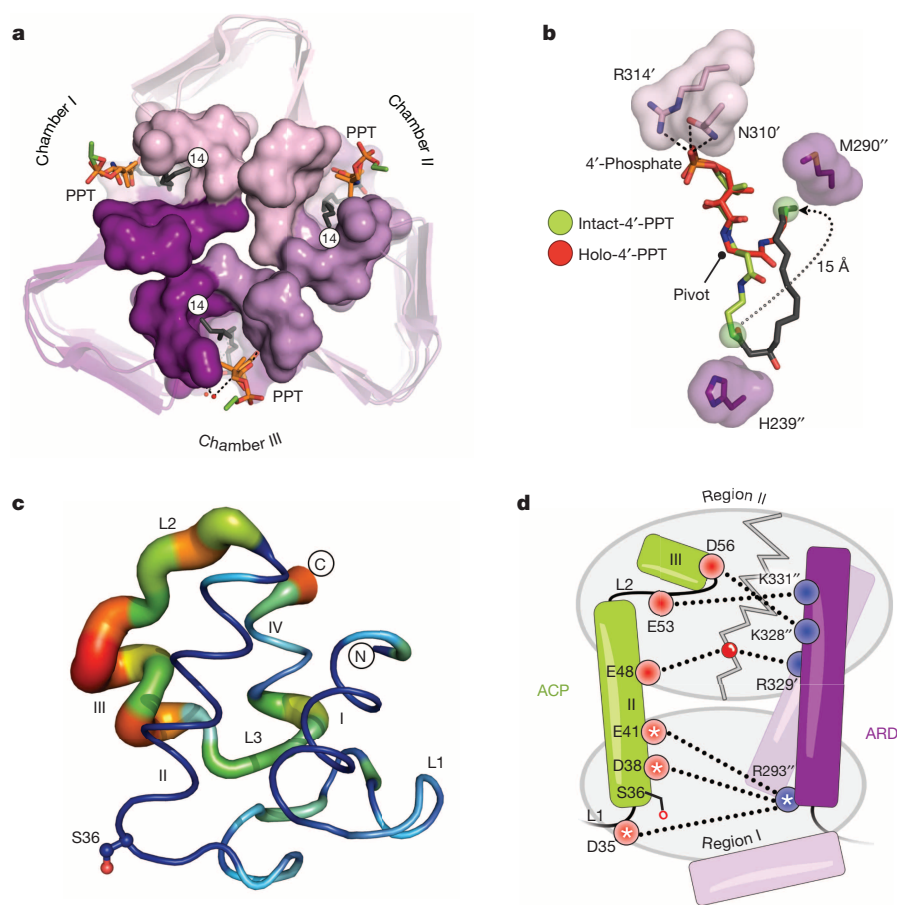
Figure 3 | ACP conformations and reorganization of its prosthetic group. a, Top-down view of LpxD (intact-acyl-ACP depicted) showing three reaction chambers enclosed by the 4′-PPT. **b,** Structural comparison between the intact- (green) and holo-4′-PPT (red) prosthetic groups. The 4′-PPT rearrangement is indicated (grey dotted arrow). **c,** Difference distance matrix calculated between fully modelled intact- (chain K) and holo-ACP (chain G). Deviations between like atoms are shown as a putty-sausage representation. Both the thickness and heat-map colouring indicate regions of least (thin, blue) to highest (thick, red) displacement. **d,** Schematic summarizing differences in electrostatic interactions between ACP complexes. Residues are indicated as red (acidic) or blue (basic) circles and subdivided according to region I or II affiliation. Interactions made by intact-acyl-ACP alone are depicted (dotted lines) and those common among all complexes are represented with a star. The grey zigzag indicates those electrostatic interactions that are broken in the hydrolysed- and holo-ACP product complexes.

holo-ACP within the asymmetric unit is displaced from the others and possibly represents a different binding state showing extra interactions that must break for dissociation (Supplementary Fig. 13).

The structures captured in this study begin to establish key molecular movements within ACP that initiate molecular recognition and a mechanism with which associations can be ultimately broken. In this context, we present a model for ACP-based synthesis of lipid A precursors catalysed by LpxD (Fig. 4) and can begin to extract some general principles for these types of interaction. First, although there does not yet seem to be a consensus-sequence binding motif on the surface
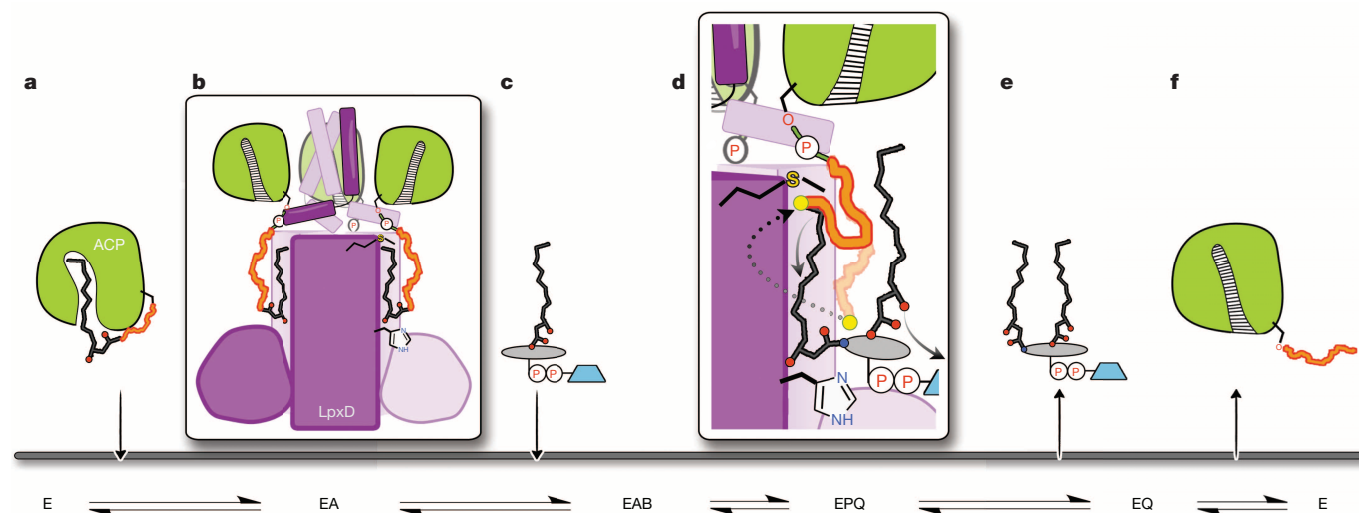
Figure 4 | Molecular basis for the ordered-sequential reaction mechanism and involvement of ACP in lipid-product release. a, b, Acyl-ACP (**a**) binds first to free LpxD forming the binary complex (**b**). ACP associates with the ARD and the acyl-4′-PPT packs into the hydrophobic N-channel. **c,** UDP-acyl-GlcN binds next, which initiates acyl transfer. **d,** In the ternary product complex the 4′-PPT arm of hydrolysed-acyl-ACP (transparent orange squiggle) completely encloses the reaction chamber, blocking UDP-diacyl-GlcN from leaving. By moving the 4′-PPT (dark orange squiggle) towards Met 290 (dotted arrow), the catalytic chamber opens up. **e, f,** This motion drives the eventual release of UDP-diacyl-GlcN (**e**) and 'triggers' conformational changes downstream of helix-II leading to holo-ACP dissociation (**f**).

of partner proteins, both regions I and II of ACP seem to be frequently involved, with most of the small number of other ACP-based complexes determined showing that helices II, -III, L1 and L2 are consistently used[22,23,26,27]. Second, because these regions are broadly universal, exploiting specific residue contacts at the interface and fine-tuning the buried surface area at these regions probably dictate how ACP-based associations can be both specific and temporary. For instance, our structures show the first direct, electrostatic coordination with the 4′-phosphate of both acyl- and holo-ACP, which in addition to extensive protein–protein contacts provide the 'strong, transient' nature of the ACP–LpxD complex. Third, because we observe ACP tied to an entire catalytic cycle, a substantial conformational change downstream of the recognition helix-II may represent a more general communication mechanism for breaking ACP–partner complexes. Finally, the stalled ACPs captured herein have shown an unprecedented role for carrier proteins in product release, and the contribution of the pantetheinyl group in both the formation and dissociation of the ACP–partner complex. Perhaps motion of the pantetheinyl group in other ACP-based complexes provokes dissociation in a similar manner, especially when considering other 'strong, transient' protein partners.

METHODS SUMMARY

Key to capturing ACP bound to LpxD at different stages of catalysis was the ability to preload *E. coli* ACP with its 4′-PPT prosthetic group by co-expression with holo-ACP synthase (ACPS), and subsequently charging holo-ACP with *R*-3-hydroxymyristic acid enzymatically using the soluble form of acyl-ACP synthetase from *Vibrio harveyi*. Holo-ACP was purified by nickel affinity, anion exchange, covalent chromatography, which exploits disulphide bond formation between the 4′-PPT group and ThioPropyl Sepharose resin (Sigma-Aldrich), and finally size-exclusion chromatography. Complete conversion of holo-ACP to its acylated form was confirmed by mass spectrometry and 2.5 M urea gel electrophoresis. The resulting acyl-ACP mixture was purified to homogeneity using size-exclusion chromatography. *E. coli* LpxD was overexpressed, and purified as previously reported[12]. An active site mutant of LpxD was also necessary to preserve the thioester bond of acyl-ACP and was generated by introducing an alanine substitution for His 239. Crystals of the complexes were grown by vapour diffusion and incubating either holo- or acyl-ACP with LpxD in a 1:1 (mol:mol) stoichiometry. Diffraction data were collected on the SER-CAT 22-BM and 22-ID beamlines at the Advanced Photon Source at Argonne National Laboratory. The structures were solved by the molecular replacement method using the published *E. coli* LpxD structure (Protein Data Bank 3EH0)[19] as the search model. *E. coli* ACP was intentionally omitted during molecular replacement and, instead, was manually rebuilt into unbiased difference electron density maps. The rate of LpxD catalysed conversion of [α-^{32}P]UDP-3-acylGlcN to [α-^{32}P]UDP-2,3-diacylGlcN was measured as described previously using thin-layer chromatography[25]. Details of all procedures are presented in Supplementary Information.

1. Butland, G. *et al.* Interaction network containing conserved and essential protein complexes in *Escherichia coli. Nature* **433**, 531–537 (2005).
2. Byers, D. M. & Gong, H. Acyl carrier protein: structure-function relationships in a conserved multifunctional protein family. *Biochem. Cell Biol.* **85**, 649–662 (2007).
3. White, S. W., Zheng, J., Zhang, Y. M. & Rock. The structural biology of type II fatty acid biosynthesis. *Annu. Rev. Biochem.* **74**, 791–831 (2005).
4. Galloway, S. M. & Raetz, C. R. H. A mutant of *Escherichia coli* defective in the first step of endotoxin biosynthesis. *J. Biol. Chem.* **265**, 6394–6402 (1990).
5. Belunis, C. J., Clementz, T., Carty, S. M. & Raetz, C. R. H. Inhibition of lipopolysaccharide biosynthesis and cell growth following inactivation of the kdtA gene in *Escherichia coli. J. Biol. Chem.* **270**, 27646–27652 (1995).
6. Poltorak, A. *et al.* Defective LPS signaling in C3H/HeJ and C57BL/10ScCr mice: mutations in Tlr4 gene. *Science* **282**, 2085–2088 (1998).
7. Akira, S., Uematsu, S. & Takeuchi, O. Pathogen recognition and innate immunity. *Cell* **124**, 783–801 (2006).
8. Onishi, H. R. *et al.* Antibacterial agents that inhibit lipid A biosynthesis. *Science* **274**, 980–982 (1996).
9. Williams, A. H., Immormino, R. M., Gewirth, D. T. & Raetz, C. R. H. Structure of UDP-N-acetylglucosamine acyltransferase with a bound antibacterial pentadecapeptide. *Proc. Natl Acad. Sci. USA* **103**, 10877–10882 (2006).
10. Jenkins, R. J. & Dotson, G. D. Dual targeting antibacterial peptide inhibitor of early lipid A biosynthesis. *ACS Chem. Biol.* **7**, 1170–1177 (2012).
11. Raetz, C. R. H., Reynolds, C. M., Trent, M. S. & Bishop, R. E. Lipid A modification systems in Gram-negative bacteria. *Annu. Rev. Biochem.* **76**, 295–329 (2007).
12. Bartling, C. M. & Raetz, C. R. H. Steady-state kinetics and mechanism of LpxD, the N-acyltransferase of lipid A biosynthesis. *Biochemistry* **47**, 5290–5302 (2008).
13. Leibundgut, M., Jenni, S., Frick, C. & Ban, N. Structural basis for substrate delivery by acyl carrier protein in the yeast fatty acid synthase. *Science* **316**, 288–290 (2007).
14. Nooren, I. M. & Thornton, J. M. Diversity of protein-protein interactions. *EMBO J.* **22**, 3486–3492 (2003).
15. Chan, D. I. & Vogel, H. J. Current understanding of fatty acid biosynthesis and the acyl carrier protein. *Biochem. J.* **430**, 1–19 (2010).
16. Ploskon, E. *et al.* Recognition of intermediate functionality by acyl carrier protein over a complete cycle of fatty acid biosynthesis. *Chem. Biol.* **17**, 776–785 (2010).
17. Roujeinikova, A. *et al.* Structural studies of fatty acyl-(acyl carrier protein) thioesters reveal a hydrophobic binding cavity that can expand to fit longer substrates. *J. Mol. Biol.* **365**, 135–145 (2007).
18. Buetow, L., Smith, T. K., Dawson, A., Fyffe, S. & Hunter, W. N. Structure and reactivity of LpxD, the N-acyltransferase of lipid A biosynthesis. *Proc. Natl Acad. Sci. USA* **104**, 4321–4326 (2007).
19. Bartling, C. M. & Raetz, C. R. H. Crystal structure and acyl chain selectivity of *Escherichia coli* LpxD, the N-acyltransferase of lipid A biosynthesis. *Biochemistry* **48**, 8672–8683 (2009).
20. Raetz, C. R. H. & Roderick, S. L. A left-handed parallel β helix in the structure of UDP-N-acetylglucosamine acyltransferase. *Science* **270**, 997–1000 (1995).
21. Frederick, A. F., Kay, L. E. & Prestegard, J. H. Location of divalent ion sites in acyl carrier protein using relaxation perturbed 2D NMR. *FEBS Lett.* **238**, 43–48 (1988).
22. Cryle, M. J. & Schlichting, I. Structural insights from a P450 carrier protein complex reveal how specificity is achieved in the P450(Biol) ACP complex. *Proc. Natl Acad. Sci. USA* **105**, 15696–15701 (2008).
23. Parris, K. D. *et al.* Crystal structures of substrate binding to *Bacillus subtilis* holo-(acyl carrier protein) synthase reveal a novel trimeric arrangement of molecules resulting in three active sites. *Structure* **8**, 883–895 (2000).
24. Kraut, D. A., Carroll, K. S. & Herschlag, D. Challenges in enzyme mechanism and energetics. *Annu. Rev. Biochem.* **72**, 517–571 (2003).
25. Kelly, T. M., Stachula, S. A., Raetz, C. R. & Anderson, M. S. The firA gene of *Escherichia coli* encodes UDP-3-O-(R-3-hydroxymyristoyl)-glucosamine N-acyltransferase. The third step of endotoxin biosynthesis. *J. Biol. Chem.* **268**, 19866–19874 (1993).
26. Agarwal, V., Lin, S., Lukk, T., Nair, S. K. & Cronan, J. E. Structure of the enzyme-acyl carrier protein (ACP) substrate gatekeeper complex required for biotin synthesis. *Proc. Natl Acad. Sci. USA* **109**, 17406–17411 (2012).
27. Babu, M. *et al.* Structure of a SLC26 anion transporter STAS domain in complex with acyl carrier protein: implications for *E. coli* YchM in fatty acid metabolism. *Structure* **18**, 1450–1462 (2010).
28. Holak, T. A., Nilges, M., Prestegard, J. H., Gronenborn, A. M. & Clore, G. M. Three-dimensional structure of acyl carrier protein in solution determined by nuclear magnetic resonance and the combined use of dynamical simulated annealing and distance geometry. *Eur. J. Biochem.* **175**, 9–15 (1988).
29. Roujeinikova, A. *et al.* X-ray crystallographic studies on butyryl-ACP reveal flexibility of the structure around a putative acyl chain binding site. *Structure* **10**, 825–835 (2002).

Author Contributions A.M., C.R.H.R. and C.W.P. designed research; A.M. performed all biochemical experiments under the guidance of C.R.H.R., P.Z. and C.W.P.; A.M. performed all protein expression, purification and crystallization; A.M. and C.W.P. contributed to data collection, structure solution and refinement; A.M., C.R.H.R. and C.W.P. analysed and interpreted the structures; A.M. and C.W.P. made the figures and wrote the manuscript; A.M., C.R.H.R., P.Z. and C.W.P. discussed the results and commented on the manuscript.

Author Information Molecular coordinates and structure factors of intact-acyl-ACP, hydrolysed-acyl-ACP and holo-ACP in complex with LpxD have been deposited in the Protein Data Bank under accession numbers 4IHF, 4IHG and 4IHH, respectively. Reprints and permissions information is available at www.nature.com/reprints. The authors declare no competing financial interests. Readers are welcome to comment on the online version of the paper. Correspondence and requests for materials should be addressed to C.W.P. (charles.pemble@duke.edu).

METHODS

Expression and purification of His₆-LpxD. *E. coli* LpxD was overexpressed, and purified as previously reported[12]. Briefly, His₆-LpxD was expressed in *E. coli* Rosetta/pLysS. The membrane-free fraction was loaded onto a 5 ml Ni-NTA (Qiagen) column and eluted in one step with 200 mM imidazole. The His₆-tag was left intact and the resulting LpxD was concentrated to approximately 4–10 ml and loaded onto a High Load 26/60 Superdex 200 gel filtration column (GE) equilibrated with 10 mM Tris-HCl, pH 7.5, 500 mM NaCl and 1 mM DTT. The protein peak had an elution profile consistent with that of the LpxD homotrimer. Fractions were pooled and concentrated to approximately 40 mg ml⁻¹ and stored in aliquots at −80 °C. The wild-type LpxD enzyme used in the LpxD assay was purified and stored in the absence of DTT.

Construction, expression and purification of His₆-LpxD point mutants. Site-directed mutants designed to alter Met 290 (Met290Cys), and His 239 (His239Ala) were accomplished using the QuikChange PCR mutagenesis kit (Stratagene). The LpxD variants were recombinantly expressed in C41(DE3) *E. coli* cells and purified in the same manner as described for wild-type His₆-LpxD. The His239Ala LpxD was stored in 10 mM Tris-HCl, pH 7.5, 500 mM NaCl and 1 mM TCEP, and Met290Cys LpxD was purified and stored in the absence of a reductant.

In vitro assay of LpxD. The LpxD catalysed conversion of [α-³²P]UDP-3-acylGlcN to [α-³²P]UDP-2,3-diacylGlcN was monitored by thin-layer chromatography as previously reported[25]. The 20 µl assay mixture containing 40 mM HEPES (pH 7.4), 0.02 mg ml⁻¹ BSA, 1.4 nM pure wild-type *E. coli* LpxD (or 4.2 nM Met290Cys LpxD), 6 µM *R*-3-hydroxymyristoyl-ACP (β-OH-C14-ACP) and 4 µM [α-³²P]UDP-3-*O*-(β-OH-C14)-GlcN (0.005–0.04 µCi µl⁻¹) was equilibrated at 30 °C, and the reaction was initiated by the addition of the enzyme. DTT (100 mM) was added to assess its effect on the catalysis of the wild-type and mutant LpxD. A 1 µl aliquot of the reaction mixture was spotted onto a silica gel 60 plate (EMD Chemicals) at various time-points. After drying under a cold air stream, plates were developed with a chloroform/methanol/water/acetic acid solvent (25:15:4:2, v:v:v:v). The plates were dried and exposed overnight to a Molecular Dynamics PhosphorImager Screen. The conversion rate of the lipid substrate to product was measured using ImageQuant software.

Expression and purification of holo-ACP. The *acp* gene was amplified from *E. coli* W3110A genomic DNA using the ACP-forward and ACP-reverse primers (Supplementary Table 1) engineered to introduce downstream of the ACP coding region a spacer sequence, a ribosome binding site, followed by a translation spacer element (denoted PCR product A). The ACPS-forward and ACPS-reverse primers (Supplementary Table 1) were used to amplify the *acps* gene from W3110A genomic DNA, which contained a spacer sequence, a ribosome binding site and a translation spacer element upstream of the ACPS coding region (denoted PCR product B). The ACP-forward and ACPS-reverse primers were subsequently used to generate PCR product C, which contained *acp* and *acps* genes separated by the spacer sequence, ribosome binding site and the translation spacer element. PCR product C was cloned into a pET16b* vector, which contained an engineered tobacco etch virus (TEV) protease cleavage site instead of Factor Xa, using the NdeI and XhoI restriction sites. *E. coli* DH5α-competent cells were subsequently transformed with plasmid and transformants were selected at 37 °C on a LB-agar plate supplemented with 100 µg ml⁻¹ ampicillin. The sequence of the plasmid encoding the N-terminally histidine-tagged ACP and non-tagged ACPS (pET16b*-AM) was confirmed by DNA sequencing.

ACP and ACPS were co-expressed using the pET16b*-AM vector in C41(DE3) *E. coli* cells and cultured at 37 °C in 1 litre of LB broth supplemented with 100 µg ml⁻¹ ampicillin. Upon reaching an absorbance at 600 nm of 0.6, the expression was induced for 6 h with 1 mM isopropyl-β-D-thiogalactopyranoside (IPTG) at 30 °C. All the subsequent procedures were performed at 4 °C. The cells were collected, washed, re-suspended and lysed in 20 mM HEPES, pH 8.0 containing 10% glycerol, 200 mM NaCl and 2 mM DTT (buffer A), supplemented with 20 mM imidazole. After removal of cell debris by centrifugation at 100,000g for 1 h, the soluble fraction was loaded onto a Ni-NTA (Qiagen) column equilibrated with buffer A and 20 mM imidazole. The Ni-NTA column was washed with 10 column-volumes and His₁₀-ACP was eluted in one step by buffer A supplemented with 250 mM imidazole over the equivalent of five column-volumes. Although ACPS was not histidine-tagged, it co-purified with His₁₀-ACP. The elution fraction was allowed to slowly rock with 1 mg of TEV protease and 2 mM EDTA overnight. Subsequently, the protein mixture was dialysed against 20 mM MES, pH 6.0 and 2 mM DTT overnight. The TEV protease and residual His₁₀-ACP were removed by passing the mixture through a 2 ml Ni-NTA column. The resulting flow-through fraction containing ACP was loaded onto a 5 ml QFF ion exchange column (GE). ACP was eluted separately from ACPS by applying a linear gradient of 20 mM MES, pH 6.0, 0–500 mM NaCl and 2 mM DTT over 50 column-volumes. The fractions corresponding to ACP were pooled together and dialysed against 100 mM Tris-HCl, pH 7.1 and 200 mM NaCl (buffer B) overnight. Holo-ACP was

separated from residual apo-ACP by mixing the ACP sample with 5 ml of ThioPropyl Sepharose 6b resin (Sigma-Aldrich) overnight. Apo-ACP, which lacks any free thiol group, did not bind to the resin, whereas holo-ACP covalently attached to the resin by the terminal thiol group of its phosphopantetheine moiety. After washing the Thiopropyl Sepharose 6b with 25 ml of buffer B, holo-ACP was eluted in 25 ml of buffer B supplemented with 25 mM DTT. The complete removal of apo-ACP was confirmed by electrospray ionization mass spectrometry. The elution fraction was concentrated to approximately 4–10 ml and loaded onto a High Load 26/60 Superdex 200 gel filtration column equilibrated with 10 mM Tris-HCl, pH 7.5, 200 mM NaCl and 2 mM DTT. The relevant eluted fractions were concentrated to approximately 20 mg ml⁻¹ and stored in aliquots at −80 °C.

Production of β-OH-C14-ACP. Holo-ACP was charged enzymatically with *R*-3-hydroxymyristic acid (Santa Cruz Biotechnology) by soluble acyl-ACP synthetase from *V. harveyi*[30]. The soluble acyl-ACP synthetase (*aasS*) gene was synthesized by GenScript. The *aasS* gene was subcloned into pET-16b expression vector, over-expressed, and the His₆-AasS was purified using nickel affinity chromatography as reported by Jiang *et al.*[30]. To generate β-OH-C14-ACP, 0.1 mM of holo-ACP was mixed with 0.001 mM AasS and 0.3 mM of the fatty acid (β-OH-C14) at room temperature for 3 h in a buffer containing 100 mM Tris-HCl, pH 7.8, 10 mM ATP and 10 mM MgCl₂. To separate acyl-ACP from AasS, the reaction mixture was loaded onto a High Load 26/60 Superdex 200 gel filtration column equilibrated with 10 mM Tris-HCl, pH 7.5 and 200 mM NaCl. The complete conversion of holo-ACP to β-OH-C14-ACP was confirmed both by electrospray ionization mass spectrometry and 2.5 M urea (19%) polyacrylamide (pH 9.5) gel electrophoresis[31].

Crystallization and structure determination. Before crystallization, either acyl-ACP or holo-ACP was mixed with the wild-type or the catalytically inactive His239Ala LpxD to preform the protein–protein complex. Crystals of holo-ACP–LpxD were grown at 15 °C by mixing the protein solution with the precipitant (0.1 M MES pH 6.0, 0.2 M lithium sulphate, 20% PEG 4000) in ratios of 1:1 and 1:1.5. Crystals achieved full size in approximately 45 days. The crystals were transferred to a cryo-solution using a 50:50 ratio of paratone to mineral oil and immediately cryo-cooled to −180 °C in liquid nitrogen. Hydrolysed-acyl-ACP–LpxD crystals were obtained by equilibrating the protein mixture against a well solution containing 0.1 M MES pH 6.5, 0.2 M ammonium sulphate, 20% PEG 8000 and incubating at 15 °C. The crystals were collected on day 10 and cryo-cooled using a solution containing ammonium sulphate, 33% PEG 8000, 5 mM Tris-HCl pH 7.5, 190 mM NaCl and 20% of the cryoprotectant ethylene glycol. To trap the intact-acyl-ACP–LpxD complex the His239Ala-LpxD mutant was purified in the presence of the reducing agent TCEP instead of DTT in an attempt to reduce hydrolysis of the thioester bond. His239Ala-LpxD and acyl-ACP were pre-mixed using a 1:1 molar ratio before crystallization trials. The well solution and the cryoprotectant were the same as that described for the hydrolysed-acyl-ACP structure; however, a ratio of 1.5:1 of protein to well solution was required.

The diffraction data were collected on the SER-CAT 22-BM and 22-ID beamlines at the Advanced Photon Source at Argonne National Laboratory. Data were processed using the HKL2000[32] software suite (Supplementary Table 2). Although the data for both intact- and holo-ACP complexes were processed to 2.1 and 2.13 Å, respectively, the hydrolysed-acyl-ACP complex was trimmed to 2.9 Å owing to the data completeness being unsatisfactory in higher resolution bins (that is, well below 70%). This resulted in a higher signal-to-noise ratio in the 2.9 Å resolution bin as well as a much lower R_{merge} value. The crystals of each complex belong to the P1 space group. The structures were solved by the molecular replacement method using the program PHASER in the PHENIX software suite[33,34] and the previously determined *E. coli* LpxD structure (Protein Data Bank 3EH0)[19] as the search model. Two trimers of LpxD were observed in the triclinic unit cell for the intact-acyl-ACP, hydrolysed-acyl-ACP and holo-ACP co-crystal structures. In each case, however, ACP was intentionally omitted during the molecular replacement process; instead, it was manually rebuilt into unbiased, contiguous $F_o − F_c$ difference electron density by first rigid-fitting the *E. coli* apo-ACP coordinates (Protein Data Bank 1T8K)[35] into the resulting maps. The models were rebuilt using COOT[36] and iterative structure refinement with restrained and TLS options was performed using PHENIX[33]. For the lower-resolution hydrolysed-acyl-ACP structure, hydrogens were included for refinement with automated optimization of X-ray/stereochemistry and ADP weights selected. Additionally, we used the high-resolution *E. coli* apo-ACP structure (Protein Data Bank 1T8K) as a reference model. The molecular coordinates and restraints of the 4′-PPT, β-OH-C14-4′-PPT and free β-OH-C14 fatty-acid ligands were generated by using either the Dundee PRODRG2 Server[37] or PHENIX Elbow[33]. Composite omit map and simulated annealing omit map calculations were conducted using CNS[38]. The protein–ligand interactions were identified by AREAIMOL calculations in the CCP4 suite[39]. The quality of the final models was validated using MOLPROBITY[40]. The data statistics are reported in Supplementary Table 2. Molecular figures were generated using PyMOL[41].

A total of six ACP molecules were present in the intact-acyl-ACP structure (Supplementary Fig. 3). Both the hydrolysed- and holo-ACP structures showed partly bound states of ACP within two or three LpxD active sites as interpreted by the lack of contiguous electron density for most of the ACP backbone. As a result, only a portion of ACP that includes Ser 36 and its 4′-PPT prosthetic group was included in the final model: (1) hydrolysed-acyl-ACP, residues 35–44 of chain L, residues 6–15, 27–53 and 62–73 of chain I, residues 1–15 and 27–73 of chain G; (2) holo-ACP, residues 35–44 of chain H and chain L. The remaining LpxD active sites in the hydrolysed- and holo-ACP structures contain fully modelled ACPs. In all three co-crystal structures, the electron density maps indicated that the N-terminal methionine of ACP was present and forms a key lattice contact with neighbouring molecules of LpxD. Two more residues (Ser–His) in the holo-ACP structure that remain from the TEV cleavage site could also be modelled.

The observed electron density for fully modelled intact-, hydrolysed- and holo-ACPs were weaker in some regions, especially on the backside of the molecule which faces solvent; however, the placement of side-chains was apparent at the protein–protein interface (Supplementary Fig. 3). This implicates conformational heterogeneity throughout the lattice. Nonetheless, in all three co-crystal structures, electron density was apparent in every active site for all atoms of the 4′-PPT group. In both the intact- and hydrolysed-forms, pronounced electron density was also present for the β-OH-C14 acyl chains located in the N-channel. In addition, electron density indicated that the hydrolysed-acyl-ACP complex included two extra molecules of β-OH-C14 fatty acid bound to the hydrophobic O-channel, although the density was weaker towards the terminal carbon atoms of the acyl chains. To investigate the origin of this second fatty acid, we mixed acyl-ACP (12.86 mg ml^{-1}) in a 1:2.25 v:v ratio with wild-type LpxD (26.38 mg ml^{-1}) pre-incubated with 1 mM DTT in a solution that was consistent with the condition used for crystallization. The protein solution was incubated at 15 °C, and aliquots were taken at different time points and stored at −80 °C. Samples were run on a 2.5 M urea (19%) polyacrylamide (pH 9.5) gel[31], which showed that both DTT

(a known phenomenon[42]) and LpxD enhance the cleavage of the thioester bond of acyl-ACP (Supplementary Fig. 10). This observation most likely explains why free β-OH-C14 fatty acid was available to bind the O-channel of LpxD.

30. Jiang, Y., Chan, C. H. & Cronan, J. E. The soluble acyl-acyl carrier protein synthetase of *Vibrio harveyi* B392 is a member of the medium chain acyl-CoA synthetase family. *Biochemistry* **45,** 10008–10019 (2006).
31. Rock, C. O., Cronan, J. E. Jr & Armitage, I. M. Molecular properties of acyl carrier protein derivatives. *J. Biol. Chem.* **256,** 2669–2674 (1981).
32. Otwinowski, Z. & Minor, W. Processing of X-ray diffraction data collected in oscillation mode. *Methods Enzymol.* **276,** 307–326 (1997).
33. Adams, P. D. *et al.* PHENIX: a comprehensive Python-based system for macromolecular structure solution. *Acta Crystallogr. D* **66,** 213–221 (2010).
34. McCoy, A. J. *et al.* Phaser crystallographic software. *J. Appl. Cryst.* **40,** 658–674 (2007).
35. Qiu, X. & Janson, C. A. Structure of apo acyl carrier protein and a proposal to engineer protein crystallization through metal ions. *Acta Crystallogr. D* **60,** 1545–1554 (2004).
36. Emsley, P. & Cowtan, K. Coot: model-building tools for molecular graphics. *Acta Crystallogr. D* **60,** 2126–2132 (2004).
37. Schuttelkopf, A. W. & van Aalten, D. M. PRODRG: a tool for high-throughput crystallography of protein-ligand complexes. *Acta Crystallogr. D* **60,** 1355–1363 (2004).
38. Brunger, A. T. *et al.* Crystallography & NMR system: a new software suite for macromolecular structure determination. *Acta Crystallogr. D* **54,** 905–921 (1998).
39. Winn, M. D. *et al.* Overview of the CCP4 suite and current developments. *Acta Crystallogr. D* **67,** 235–242 (2011).
40. Chen, V. B. *et al.* MolProbity: all-atom structure validation for macromolecular crystallography. *Acta Crystallogr. D* **66,** 12–21 (2010).
41. DeLano, W. L. The PyMOL Molecular Graphics System v. 1.3r1 (Schrödinger, LLC, New York, New York, 2012).
42. Stokes, G. B. & Stumpf, P. K. Fat metabolism in higher plants. The nonenzymatic acylation of dithiothreitol by acyl coenzyme A. *Arch. Biochem. Biophys.* **162,** 638–648 (1974).